EDGE ARTICLE

Check for updates

A pH-responsive ultrathin Cu-based nanoplatform for specific photothermal and chemodynamic synergistic therapy†

Tingting Hu,‡[a] Liang Yan,‡[a] Zhengdi Wang,[a] Weicheng Shen,[a] Ruizheng Liang, [ID] *[a] Dongpeng Yan*[b] and Min Wei [ID] *[a]

Noninvasive tumor therapy requires a new generation of bionanomaterials towards sensitive response to the unique tumor microenvironment to achieve accurate and effective treatment. Herein, we have developed a tumor therapy nanoplatform by immobilizing natural glucose oxidase (GOD) onto Cu-based layered double hydroxide (CuFe-LDH) nanosheets, which for the first time integrates acid-enhanced photothermal therapy (PTT), and pH-responsive and heat-facilitated chemodynamic therapy (CDT) simultaneously. As demonstrated by EXAFS and HRTEM, CuFe-LDH nanosheets possess a considerable number of defects caused by different acid conditions, resulting in a significantly acid-enhanced photothermal conversion efficiency (83.2% at pH 5.4 *vs.* 46.0% at pH 7.4). Moreover, GOD/CuFe-LDH nanosheets can convert a cascade of glucose into hydroxyl radicals (˙OH) under tumor acid conditions, which is validated by a high maximum velocity ($V_{max} = 2.00 \times 10^{-7}$ M) and low Michaelis–Menten constant ($K_M = 12.01$ mM). With the combination of PTT and CDT, the tumor tissue *in vivo* is almost eliminated with low-dose drug injection (1 mg kg^{-1}). Therefore, this novel pH-responsive Cu-based nanoplatform holds great promise in tumor-specific CDT/PTT synergistic therapy.

Introduction

As one of the most serious diseases, cancer is severely threatening the health of human beings due to its high incidence and mortality.[1] Conventional cancer therapies typically include surgery, chemotherapy and radiotherapy.[2–5] However, each of these methods has its own drawbacks, such as unsatisfactory tumor elimination, poor target specificity, and serious side effects. To address these limitations, promising noninvasive therapies including photodynamic therapy (PDT), ultrasonic therapy, photothermal therapy (PTT) and chemodynamic therapy (CDT) emerged in the last few years.[6–10] PTT is a novel strategy of cancer treatment that converts near-infrared (NIR) light to heat and possesses low side effects, noninvasiveness, and high spatiotemporal selectivity.[11–14] However, due to the restriction of the heterogeneous heat distribution in tumor tissue, PTT would lead to unsatisfactory tumor ablation and

cause damage to the surrounding normal cells and tissues, and therefore is known as a non-specific treatment.[15–17] As a new type of treatment, CDT relies on the Fenton reaction to catalyze the generation of highly oxidative hydroxyl radicals (˙OH) from hydrogen peroxide (H_2O_2) to damage biomolecules (such as DNA and proteins) in cancer cells.[18–22] Since the Fenton reaction works rapidly only under acidic conditions, CDT can respond to the unique tumor microenvironment (TME) to achieve specific and selective tumor treatment, and thus avoid damage to normal tissues.[23–25] Unfortunately, the unsatisfactory H_2O_2 concentration and weak catalytic efficiency *in vivo* obviously limit the further development of CDT.[26–28] Theoretically, the heat produced by PTT can significantly improve the CDT effectiveness, and CDT can also disturb microenvironmental conditions and increase the thermal sensitivity of cancer cells, resulting in enhanced PTT efficacy.[29] Therefore, developing a specific and synergistic PTT/CDT would be a promising strategy to enhance the cancer therapeutic efficiency and minimize the damage to the surrounding healthy tissues.

Based on the theory of defect-induced photogenerated electron–hole enhancement, defect-rich nanomaterials caused by an acid environment can achieve increased PTT.[30] Thus, we aim to develop a tumor-specific synergistic therapy nanoplatform to realize acid-enhanced PTT as well as pH-responsive and PTT-enhanced CDT. Layered double hydroxides (LDHs) are a kind of two-dimensional (2D) nanomaterial with the general formula of $[M^{2+}_{1-x}M^{3+}_x(OH)_2](A^{n-})_{x/n}\cdot mH_2O$ (M^{2+} and M^{3+} represent

[a]*State Key Laboratory of Chemical Resource Engineering, Beijing Advanced Innovation Center for Soft Matter Science and Engineering, Beijing University of Chemical Technology, Beijing 100029, P. R. China. E-mail: liangrz@mail.buct.edu.cn; weimin@mail.buct.edu.cn*

[b]*Beijing Key Laboratory of Energy Conversion and Storage Materials, College of Chemistry, Beijing Normal University, Beijing 100875, P. R. China. E-mail: yandp@bnu.edu.cn*

† Electronic supplementary information (ESI) available. See DOI: 10.1039/d0sc06742c

‡ These authors contributed equally to this work.

bivalent and trivalent cations respectively, and A^{n-} acts as the exchangeable interlaminar anion and can balance the charge of the host layer), and have been widely explored as inorganic-biological composite nanomaterials due to their good biocompatibility.[6,31,32] With a uniform shape, high specific surface area and tunable chemical composition, LDHs have been demonstrated as excellent drug carriers with specific cell imaging functions. Moreover, LDHs can be reorganized to produce plenty of defects under acidic conditions, which induces photogenerated electron–hole pairs to realize efficient acid-enhanced NIR photothermal conversion.[30] Given the above properties of LDHs, if a new acid-enhanced and responsive PTT/CDT platform could be designed by introducing photothermal and chemodynamic dual-functional metal species (such as Cu^{2+} and Fe^{3+}) into the LDH matrix, the TME-responsive cancer synergistic therapy can be facilely implemented. The advantages of the ultrathin CuFe-LDH nanosheets designed here include: (1) the ultrathin nanostructure provides an ultrahigh specific surface area and rich active sites, which has great superiority in drug loading and defect preparation; (2) the cross-distribution of Cu and Fe species in host layer provides a periodic monatomic structure, which will enhance localized surface plasmon resonance and synergetic photothermal performance; (3) the abundant hydroxyl groups in the CuFe-LDH nanosheets improve the affinity toward intracellular H_2O_2 through electrostatic interaction, which obviously promotes CDT efficacy.

Herein, we designed and synthesized a multifunctional nanosystem (GOD/CuFe-LDHs) by loading natural glucose oxidase (GOD) onto CuFe-LDH nanosheets, realizing synchronous acid-enhanced/responsive CDT/PTT synergistic treatment (Scheme 1). With a lateral size of ~65 nm and a thickness of ~1.3 nm determined by HTEM and AFM, CuFe-LDHs catalyzed the release of highly toxic ·OH from H_2O_2 through the Fenton reaction. Moreover, as an enzyme catalyst, GOD could deplete glucose to produce abundant H_2O_2 in the acidic TME, thus effectively solving the problem of limited H_2O_2 concentration. Furthermore, GOD/CuFe-LDHs possessed an acid-enhanced NIR photothermal treatment effect based on the defect-induced increase of photogenerated electron–hole pairs. The photothermal conversion efficiency (PCE) was 83.2% at pH = 5.4, which was higher than that of most state-of-the-art nanoparticle-based systems (Table S1†).[29,33–40] The local heat generated from PTT further accelerated the activity of the Fenton reaction, resulting in highly efficient CDT. Both *in vitro* and *in vivo* tests displayed significant cell apoptosis and tumor growth suppression after being treated with GOD/CuFe-LDHs plus irradiation, indicating an excellent synergistic CDT/PTT effect. Therefore, this work provides an effective and easily scalable way to integrate CDT and PTT within the same nanoplatform for high-efficiency tumor-specific therapy.

Results and discussion

CuFe-LDH nanosheets were synthesized *via* a "bottom-up" method that provides great advantages such as finely controlled structures (uniform shapes and high surface volume ratios) and superior functions. High-resolution transmission electron microscopy (HRTEM) images in Fig. 1A show that the lateral size of the obtained CuFe-LDH nanosheets was approximately 65 nm with a monodispersed hexagonal shape morphology, and the lattice fringe spacing of the LDH (110) plane was 0.154 nm. The hydrodynamic diameter of CuFe-LDH nanosheets was 65 ± 5 nm in water as determined by the dynamic light scattering (DLS) method (Fig. S1†), which was consistent with HRTEM observations. Moreover, the homogeneous distribution of Cu and Fe throughout the LDH matrix was evidenced by energy-dispersive X-ray (EDX) mapping (Fig. 1B). Atomic force microscopy (AFM) images of CuFe-LDH nanosheets displayed
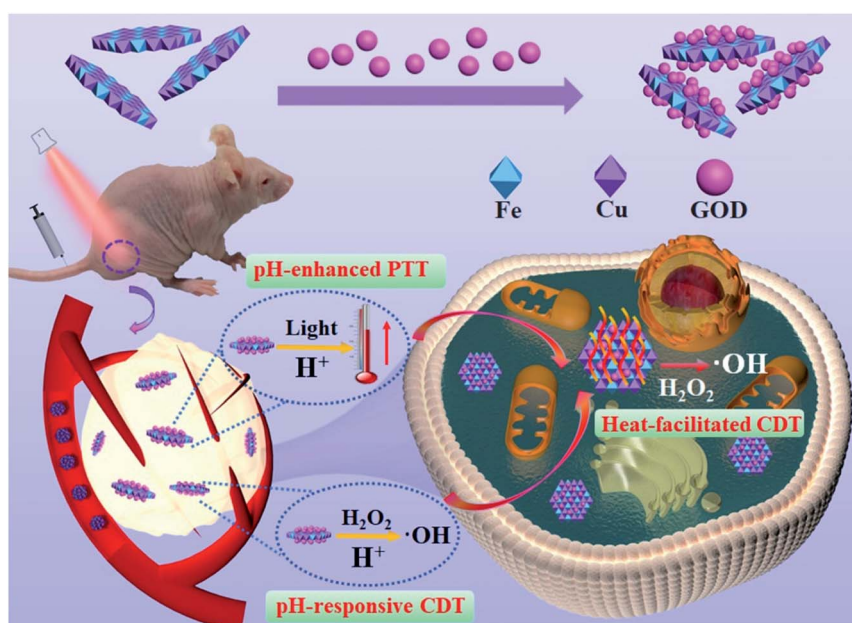
Scheme 1 A schematic illustration of the tumor-specific therapy mechanism in the presence of GOD/CuFe-LDHs.
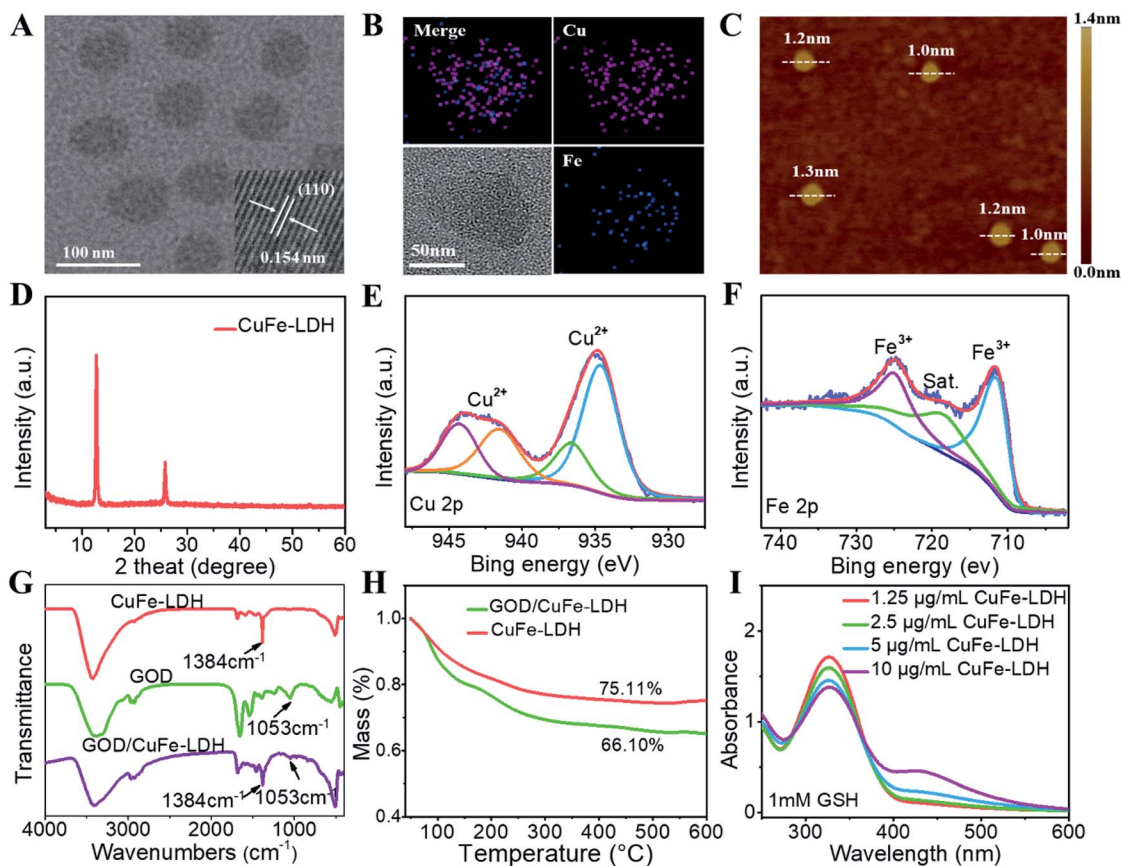
Fig. 1 (A) HRTEM image and (B) EDX mapping of CuFe-LDH nanosheets. (C) AFM image of CuFe-LDH nanosheets. (D) XRD patterns of CuFe-LDHs. XPS spectra of (E) Cu 2p and (F) Fe 2p. (G) FT-IR spectra of CuFe-LDHs, GOD and GOD/CuFe-LDHs. (H) Thermogravimetric curves of CuFe-LDH and GOD/CuFe-LDH nanosheets respectively at a temperature from 298 K to 873 K. (I) The UV absorbance spectra of the reaction of DTNB with GSH in the presence of CuFe-LDHs with different concentrations (1.25–10 μg mL^{-1}).

a thickness of ~1.3 nm (Fig. 1C), indicating the uniformly ultrathin nanostructure.[41] Such 2D nanosheets would facilitate biocompatibility with cells. The X-ray diffraction (XRD) analysis revealed a diffraction peak at $2\theta = 12.24°$, in accordance with the characteristic (003) reflection of the LDH phase (Fig. 1D). In addition, the chemical state of Cu and Fe in CuFe-LDHs was confirmed by X-ray photoelectron spectroscopy (XPS). Fig. 1E shows Cu 2p characteristic peaks at 934.69 eV (2p3/2) and 944.31 eV (2p1/2), indicating the appearance of the Cu^{2+} state in CuFe-LDHs. In the Fe 2p spectrum, two main characteristic peaks were observed at 711.68 eV (2p3/2) and 725.19 eV (2p1/2) (Fig. 1F), confirming the Fe^{3+} species within CuFe-LDH nanosheets.

The loading of GOD onto CuFe-LDH nanosheets was further studied. Fourier transform infrared (FT-IR) spectra were recorded to prove the combination of GOD and CuFe-LDHs (Fig. 1G), in which the absorption peak at 1384 cm^{-1} (symmetric stretching vibration of N–O) of NO_3^- in LDHs and absorption band at 1053 cm^{-1} (stretching vibration of C–OH) of GOD were detected in the GDO/CuFe-LDH nanosheets, indicating that GOD was successfully loaded onto CuFe-LDH nanosheets. As shown in Fig. S2,† the zeta potential of CuFe-LDH, GOD and GOD/CuFe-LDH samples was measured to be 26.3, −19.8 and 15.6 mV respectively, further confirming the assembly of GOD onto CuFe-LDHs. The hydrodynamic diameter of GOD/CuFe-LDH nanosheets measured by DLS was 70 ± 5 nm in water (Fig. S3†), and the GOD/CuFe-LDH nanosheets possessed excellent dispersion stability with an unchanged hydrodynamic diameter within one week (Fig. S4†). Moreover, the loading amount of CuFe-LDH nanosheets toward GOD was measured by thermogravimetry (TG), which was determined to be 9.01% according to the weight loss curve of CuFe-LDHs and GOD/CuFe-LDHs (Fig. 1H).

GSH, a reducing substance that exists in cancer cells, can recognize the reactive oxygen species (ROS) produced by the Fenton reaction to greatly reduce the efficiency of CDT.[42] We firstly investigated the regulating ability of GOD/CuFe-LDHs toward GSH depletion by the DTNB assay. GOD/CuFe-LDHs of different concentrations (1.25–10 μg mL^{-1}) was added to 1 mM GSH aqueous solution, and the absorbance of DTNB decreased as the GOD/CuFe-LDH concentration increased (Fig. 1I), indicating that GSH could be consumed by GOD/CuFe-LDHs. To further verify the reaction between GSH and GOD/CuFe-LDHs, XPS was utilized to study the change in the state of Cu and Fe in CuFe-LDHs after the reaction. As shown in the XPS spectra (Fig. S5†), some Cu^{2+} and Fe^{3+} were reduced to Cu^+ and Fe^{2+} in the presence of GSH, which significantly reduced the antioxidant capacity of the tumor. The above-mentioned results show
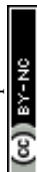
that GOD/CuFe-LDHs can regulate the GSH level in the TME, which will further lead to enhanced CDT performance.

The UV-vis-NIR spectra of GOD/CuFe-LDH nanosheets at different pH values were further investigated. As displayed in Fig. 2A–C, the GOD/CuFe-LDH suspension exhibited obvious absorption between 600 nm and 900 nm, indicating that CuFe-LDHs could absorb NIR at 808 nm. The absorbance intensity of GOD/CuFe-LDH nanosheets at pH = 7.4 increased linearly with the increase of concentration. However, the absorbance of GOD/CuFe-LDH samples at pH = 6.5 and 5.4 shifted from a wide range to an absorption peak around 750 nm. This change could be ascribed to the local erosion of GOD/CuFe-LDH nanosheets under weak acid conditions, and similar results have been reported in previous studies.[49] Subsequently, the temperature change of GOD/CuFe-LDH samples at different pH values was monitored under the irradiation of an 808 nm laser (1.0 W cm^{-2}). The temperature of GOD/CuFe-LDHs (100 μg mL^{-1}) upon 10 min irradiation increased obviously as the pH value decreased. The temperature increment (ΔT) at pH = 7.4, 6.5, 5.4 was 15.8, 25.2, and 26.6 °C respectively, while the PBS only gave a ΔT of 5.5 °C (Fig. 2D). Such results could be ascribed to the occurrence of some defects accompanying the weak acid environment that etched the surface of CuFe-LDHs, which enhanced the photogenerated electron–hole to realize efficient NIR photothermal conversion.[30] The temperature changes and thermal infrared images were measured by an IR thermal camera (Fig. 2E). The temperature of GOD/CuFe-LDHs at pH =

7.4, 6.5, 5.4 reached 44.3, 54.2 and 56.5 °C respectively, while the temperature of PBS was 37.6 °C, manifesting the excellent photothermal performance of GOD/CuFe-LDHs in weak acid environments. Moreover, the PCE of GOD/CuFe-LDH nanosheets at pH = 7.4 was determined to be 46.0% (Fig. S6†), while the PCE of GOD/CuFe-LDH nanosheets at pH = 6.5 and 5.4 significantly increased to 75.1% (Fig. 2F) and 83.2% (Fig. 2G) respectively. In addition, the photothermal conversion also indicated the linear relation of concentration and ΔT (Fig. 2H): an increase of ΔT from 13.4 °C to 35.6 °C could be obtained with an increase in concentration (25–200 μg mL^{-1}; pH = 6.5). Furthermore, photothermal stability tests showed a stable photothermal conversion capability in five successive heating/cooling cycles, indicating the repeatable and regenerated photothermal performance of GOD/CuFe-LDHs (Fig. 2I).

As a CDT reagent, CuFe-LDH nanosheets can decompose H_2O_2 through a Fenton-like reaction to generate ˙OH, which can further react with terephthalic acid (TA) to produce fluorescent 2-hydroxyterephthalic acid.[43] Hence, we utilized TA as a probe to detect the generated ˙OH. As shown in Fig. S7A and B,† the CDT performance of CuFe-LDHs in a simulated TME was assessed by adding CuFe-LDHs (50 μg mL^{-1}) to H_2O_2 (100 μM) at different pH values. The fluorescence intensity of 2-hydroxyterephthalic acid at 425 nm did not change obviously at pH = 7.4 (representing a normal tissue environment), but increased significantly with the extension of time at pH = 6.5 (representing the TME), indicating that the CDT performance of CuFe-LDHs
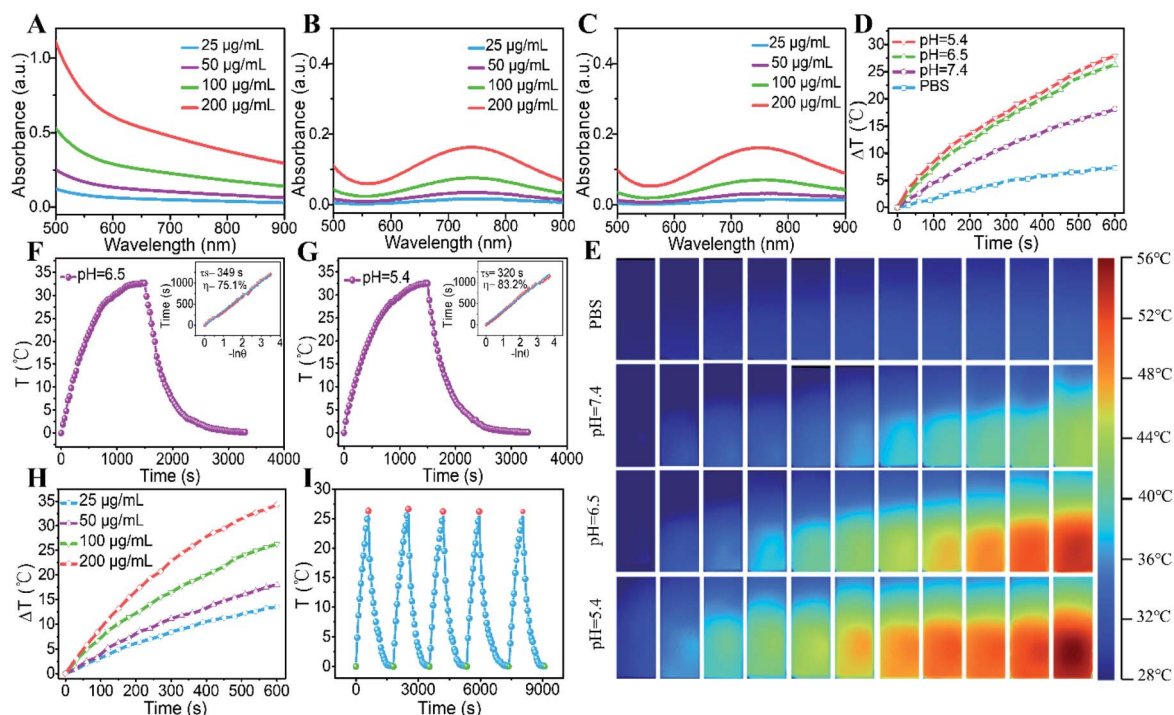

Fig. 2 (A–C) UV-vis absorbance spectra of GOD/CuFe-LDHs with different concentrations (25, 50, 100, 200 μg mL^{-1}) at pH 7.4, 6.5 and 5.4 respectively. (D) Photothermal heating curves of PBS and GOD/CuFe-LDHs at pH 7.4, 6.5 and 5.4. (E) Photothermal photographs of water and GOD/CuFe-LDHs upon 808 nm irradiation at 1.0 W cm^{-2}. Calculation of the photothermal-conversion efficiency under 808 nm irradiation at pH 6.5 (F) and 5.4 (G). (H) The photothermal effect of GOD/CuFe-LDHs with different concentrations at pH 6.5. (I) Temperature variation of GOD/CuFe-LDHs at pH 6.5 under irradiation at 1.0 W cm^{-2} for 5 light on/off cycles (10 min of irradiation for each cycle). The time constant (τ_s) for the heat transfer was calculated by applying the linear time data from the cooling period.

could only be triggered under acidic conditions. Subsequently, the CDT performance of GOD/CuFe-LDHs was further estimated by adding GOD/CuFe-LDHs (50 μg mL^{-1}) to a glucose solution (1 mM) at different pH values (Fig. S7D and E†). The results indicated that GOD/CuFe-LDHs could convert glucose into H_2O_2 and further catalyzed the decomposition of H_2O_2 to generate a large amount of ˙OH under weak acid conditions (pH = 6.5) or in a neutral environment (pH = 7.4). The CDT effect of CuFe-LDHs and GOD/CuFe-LDHs at 50 °C was further tested. As depicted in Fig. S7C, F† and 3A, B, the CDT efficiency of CuFe-LDHs and GOD/CuFe-LDHs at 50 °C was higher than that at room temperature, suggesting that CDT performance could be improved under high-temperature stimulation. These results demonstrated that GOD/CuFe-LDHs can be used as an effective PTT-enhanced CDT reagent in cancer therapy.

Electron spin resonance (ESR) spectroscopy is considered as the most effective evidence to identify ˙OH by using 5,5-dimethyl-1-pyrroline N-oxide (DMPO) as the capture probe.[44] As shown in Fig. 3C, the characteristic 1 : 2 : 2 : 1 ˙OH signal was observed when the CuFe-LDH suspension was at pH = 6.5 while the signal was inconspicuous at pH = 7.4. When the

temperature reached 323 K, a higher ˙OH signal intensity was observed in the ESR spectrum. It is noteworthy that, when glucose was introduced into the GOD/CuFe-LDH suspension, an obvious ˙OH signal at pH = 6.5 was also observed (Fig. 3D). Moreover, GOD/CuFe-LDHs at 323 K demonstrated a much stronger ˙OH generation ability than that at 298 K, confirming that GOD/CuFe-LDHs possessed a thermal-augmented effect in promoting the Fenton reaction to generate the ˙OH radical. Thus, GOD/CuFe-LDHs could effectively initiate acidity-/ temperature-responsive and glucose-triggered ˙OH generation. The underlying mechanism of the catalytic Fenton reaction was further revealed by choosing 3,3′,5,5′-tetramethylbenzidine (TMB) assay to determine the catalytic effect of GOD/CuFe-LDHs on the production of ˙OH that can oxidize TMB to blue-green TMB cation-free radicals with the maximum absorbance at 650 nm.[45] Initially, the typical enzyme-kinetics theory was adopted to explore the catalytic activity of GOD/CuFe-LDHs with H_2O_2 as the substrate. Through the Beer–Lambert law, the Michaelis–Menten curve could be used to calculate and fit the initial reaction rate, and the Michaelis constant (K_M) and the maximal reaction rate (V_{max}) of GOD/CuFe-LDHs were
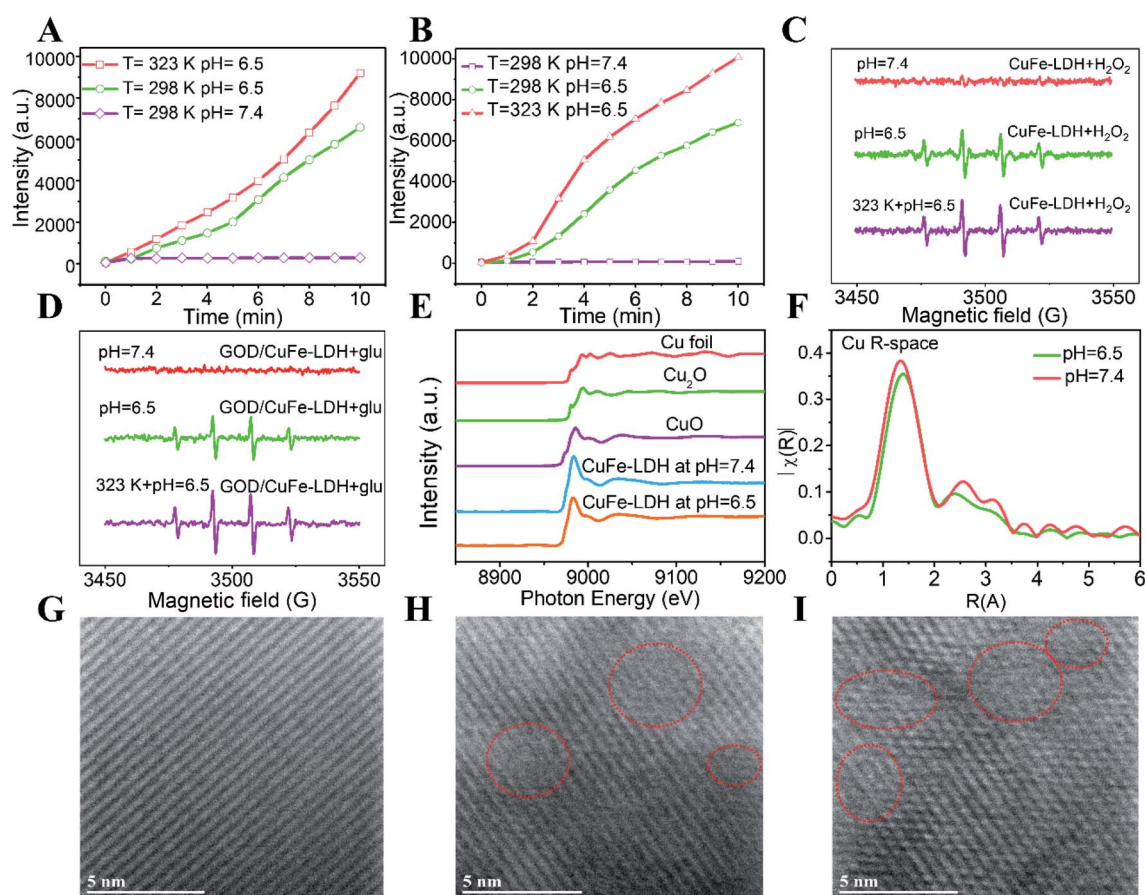

Fig. 3 The reaction of TA with the generated ˙OH-induced enhancement of fluorescence (A) CuFe-LDHs and H_2O_2 at pH = 7.4, 6.5, 6.5 + 323 K; (B) GOD/CuFe-LDHs and glucose at pH = 7.4, 6.5, 6.5 + 323 K. (C) ESR spectra of CuFe-LDHs by adding H_2O_2 in buffers at various pH values. (D) ESR spectra of GOD/CuFe-LDHs by adding glucose in buffers at various pH values. (E) Cu K-edge XANES spectra of water-plasma exfoliated CuFe-LDH nanosheets at pH 7.4 and 6.5, CuO, Cu$_2$O, and Cu foil. (F) Cu K-edge FT-EXAFS for water-plasma exfoliated CuFe-LDH nanosheets at pH 7.4 and 6.5 with homologous curve-fitting results. (G–I) Lattice fringes of CuFe-LDHs at pH 7.4, 6.5 and 5.4 respectively (red dashed circles indicate lattice defects).

calculated from the Lineweaver–Burk plot to be 13.16 mM and 1.69×10^{-7} M s^{-1} respectively (Fig. S8A–C†). Similarly, the steady-state kinetics of GOD/CuFe-LDHs was evaluated in the subsequent glucose supply experiment (Fig. S8D–F†). According to our projection, the catalytic activity of GOD/CuFe-LDHs was dependent on the glucose concentration (Fig. S8D†), and the kinetics also conformed to the Michaelis–Menten behavior (Fig. S8E†). The K_M and the V_{max} were determined to be 12.01 mM and 2.00×10^{-7} M s^{-1} respectively (Fig. S8F†). The above results guarantee a mild and stable sequential catalytic Fenton reaction of GOD/CuFe-LDHs in the TME, inducing a good anti-cancer therapeutic effect.

To better understand how different pH conditions influence local coordination structures and surface defects within CuFe-LDHs, the Cu EXAFS spectra for vacuum-dried CuFe-LDH powders at different pH values were recorded. In Fig. 3E, the main absorption edge of Cu in CuFe-LDHs at pH = 7.4 and 6.5 appeared approximately at 8995.6 eV and a weak absorption pre-edge feature was observed at 8972 eV, which was attributed to the 1s to 4p dipole transition and the 1s to 3d electronic transition respectively, indicating the presence of Cu^{2+}. In Fig. 3F, the Fourier-transformed extended X-ray absorption fine structure (FT-EXAFS) of the CuFe-LDH sample illustrated that the explicit octahedral coordination of Cu–OOH at pH = 6.5 was slightly smaller than that at pH = 7.4, which could be ascribed to the presence of oxygen vacancies at pH = 6.5. This information manifested that CuFe-LDHs at pH = 6.5 could provide more catalytically active sites to enhance Fenton reaction efficiency. In addition, lattice defects on the (110) lattice plane of CuFe-LDHs under three pH conditions were displayed using HRTEM images (Fig. 3G–I). Apparently, some defect points were observed at pH = 6.5 and 5.4, but not at pH = 7.4, demonstrating that the weak acid environment could etch the surface of CuFe-LDHs and caused some defects that are beneficial to photothermal conversion, resulting in acid-enhanced PTT performance.

In vitro anticancer performance of GOD/CuFe-LDH nanosheets was investigated through the standard methyl thiazolyl tetrazolium (MTT) assay.[46] The cytotoxicity of CuFe-LDHs in three types of cancer cells (Hela, U87MG and HepG2) was first
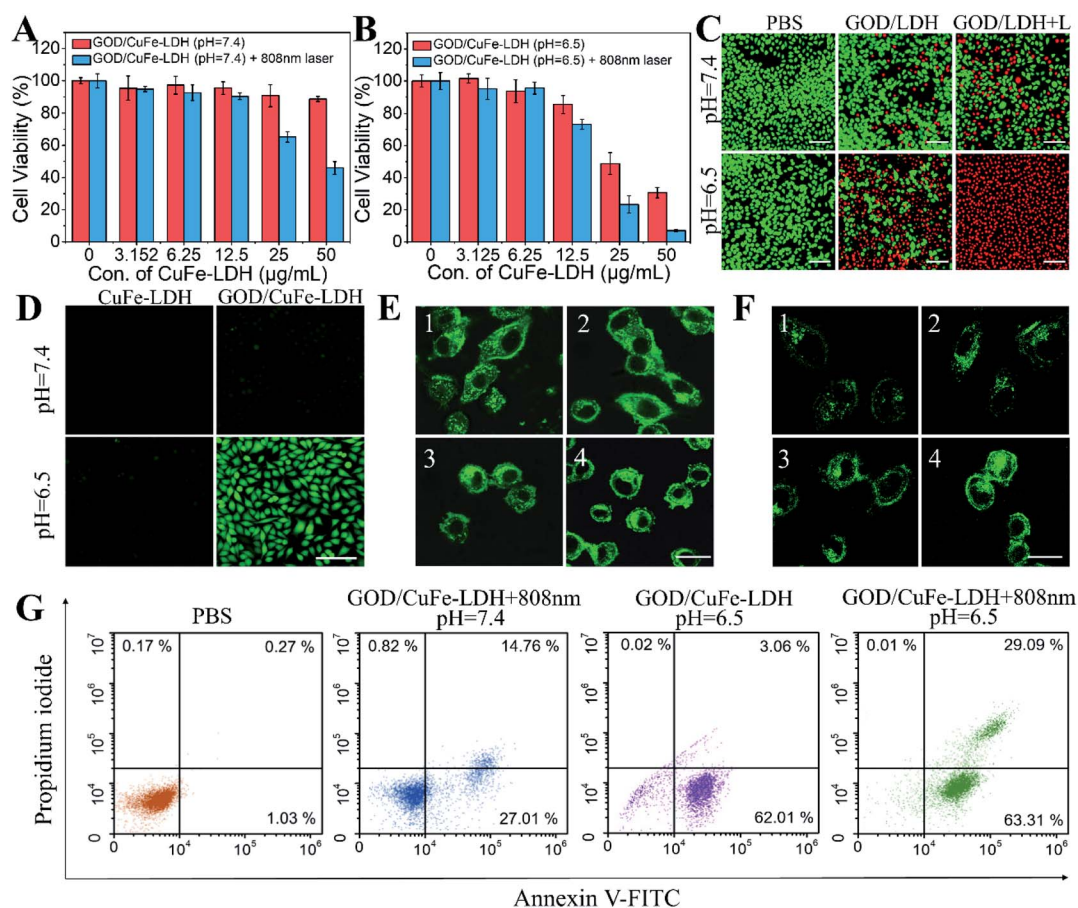

Fig. 4 Relative viability of Hela cells incubated with GOD/CuFe-LDHs under (A) neutral (pH = 7.4) and (B) acidic (pH = 6.5) conditions with and without 808 nm laser irradiation at a power density of 1.0 W cm^{-2} for 10 min, and (C) corresponding Calcein-AM/PI staining images. (D) CLSM images of Hela cells after co-incubation with CuFe-LDHs (50 μg mL^{-1}) and GOD/CuFe-LDHs (50 μg mL^{-1}) under neutral (pH = 7.4) and acidic (pH = 6.5) conditions for 6 h and subsequently stained with ROS fluorescence probe DCFH-DA. CLSM images of LysoTracker Green DND-26 (green) stained lysosome (E) and MitoTracker Green FM (green) stained mitochondria (F): (1) PBS, (2) pH 7.4 + GOD/CuFe-LDHs (50 μg mL^{-1}) + NIR (1.0 W cm^{-2}, 10 min), (3) pH 6.5 + GOD/CuFe-LDHs (50 μg mL^{-1}), (4) pH 6.5 + GOD/CuFe-LDHs (50 μg mL^{-1}) + NIR (1.0 W cm^{-2}, 10 min). (Scale bars: C, D 100 μm; E, F 25 μm.) (G) Cell apoptosis analysis using the PI/annexin V-FITC double staining method.

examined with variable concentrations from 12.5 to 200 μg mL^{-1} and the MTT results showed that the cell viability was above 95% (Fig. S9Aand B†), indicating the high biocompatibility of CuFe-LDHs. Subsequently, the synergetic PTT/CDT efficiency of GOD/CuFe-LDHs was studied and Hela cells were cultured with CuFe-LDHs and GOD/CuFe-LDHs respectively at pH = 7.4 and 6.5 for 24 h in the presence of an equivalent drug dosage ranging from 3.125 to 50 μg mL^{-1}. As illustrated in Fig. S10,† the viability of cells treated with CuFe-LDHs (50 μg mL^{-1}) without irradiation was found to be 98.7% (pH = 7.4) and 94.6% (pH = 6.5) as well as 70.9% (pH = 7.4) and 54.1% (pH = 6.5) with irradiation (1.0 W cm^{-2}, 10 min). As for GOD/CuFe-LDHs, the synergetic PTT/CDT performance enhanced obviously and the viability of cells treated with GOD/CuFe-LDHs without irradiation was found to be 88.6% (pH = 7.4) and 30.4% (pH = 6.5) as well as 45.9% (pH = 7.4) and 6.9% (pH = 6.5) with irradiation (1.0 W cm^{-2}, 10 min) (Fig. 4A and B), demonstrating that the most effective anticancer performance of GOD/CuFe-LDHs occurred at pH = 6.5 with NIR irradiation. In addition, considering that the concentration of GSH in cancer cells is usually 7–10 times higher than that in normal cells, we examined the therapeutic effect of GOD/CuFe-LDHs in a normal cell model (Cos-7: African green monkey kidney fibroblasts). In Fig. S11,† the MTT results showed that the lethality of GOD/CuFe-LDHs to Cos-7 cells was comparable to that of Hela cells under various treatments, indirectly indicating that GOD/CuFe-LDHs could effectively regulate the GSH level in cancer cells and prevent GSH from depleting ROS. Hela cells cultured with 50 μg mL^{-1} of GOD/CuFe-LDHs under the above conditions were further visualized by the calcein acetoxymethyl ester and propidium iodide (Calcein-AM/PI) method (Fig. 4C), and GOD/CuFe-LDHs at pH = 6.5 with irradiation displayed the best anticancer activity, which was in line with MTT test results. The ROS generation in cells was evaluated by selecting 2′,7′-dichlorodihydrofluorescein diacetate (DCFH-DA) as a fluorescent probe.[47] Corresponding confocal laser scanning microscopy (CLSM) images of Hela cells treated with CuFe-LDHs and GOD/CuFe-LDHs at pH = 7.4 and 6.5 were acquired (Fig. 4D), and the results revealed that cells treated with GOD/CuFe-LDHs at pH = 6.5 exhibited the strongest fluorescence signal, indicating the highest ROS production.

Cell death is often accompanied by structural damage to organelles including lysosomes and mitochondria.[48] In order to reveal the damage caused by PTT, CDT and PTT/CDT to organelles, we preliminarily investigated the effect of different treatments on lysosomes (Fig. 4E). The cells in the PBS group showed green staining spots due to the lysosomal entrapment in the cytoplasm, however, green staining spots blurred and green punctation reduced in the cells treated with GOD/CuFe-LDHs (pH 7.4) under NIR irradiation, indicating that local heat generated from GOD/CuFe-LDHs caused lysosomal damage to a certain extent. The green spots almost disappeared, and the green fluorescence intensity of cytoplasm increased obviously in the GOD/CuFe-LDH (pH = 6.5) group, indicating that ˙OH generated by GOD/CuFe-LDHs could destroy lysosomes. As for the GOD/CuFe-LDHs (pH = 6.5) in the NIR group, the strongest green fluorescence intensity was found in the

cytoplasm, indicating that CDT/PTT could cause further damage to lysosomes. To further confirm lysosomal damage, the acridine orange (AO) relocation assay was adopted to monitor the lysosomal membrane permeabilization (LMP) of Hela cells (Fig. S12†), since the hyperthermia and/or the produced ˙OH can cause lysosomal membrane destabilization. As expected, an increase in orange fluorescence of the entire cytoplasm was observed after the treatment with PTT (GOD/CuFe-LDHs (pH 7.4) under NIR irradiation), CDT (GOD/CuFe-LDHs (pH 6.5)) and synergistic PTT/CDT (GOD/CuFe-LDHs (pH 6.5) under NIR irradiation), indicating that pronounced LMP could cause the release of lysosomal content into the cytoplasm. In the PTT/CDT group, the orange fluorescence was the strongest and the nuclear morphology shrunk significantly, demonstrating the hyperthermia/˙OH-mediated lysosome destruction. Subsequently, the damage caused by PTT, CDT and PTT/CDT to mitochondria was also evaluated (Fig. 4F). The cells treated with PBS had filamentous mitochondria with green linear staining, but the mitochondria became fragmented in GOD/CuFe-LDHs (pH = 7.4) in the NIR group and GOD/CuFe-LDH (pH = 6.5) group because of the severe influence of local heat and ˙OH generation. In particular, after being treated with GOD/CuFe-LDHs (pH 6.5) under NIR irradiation, the progressive increase in treatment-induced mitochondrial fragmentation confirmed severe mitochondrial damage. The changes in mitochondrial membrane potential (MMP) were assessed by 5,5′,6,6′-tetrachloro-1,1′,3,3′-tetraethyl-imidacarbocyanine iodide (JC-1) staining (Fig. S13†). In active mitochondria, the JC-1 dyes can enter the mitochondrial matrix easily to form aggregates with red fluorescence, while in inactive mitochondria, the JC-1 dyes are not able to enter the matrix and mainly exist in the form of monomers with green fluorescence. Compared with the control group, the cells treated with GOD/CuFe-LDHs (pH 7.4) under NIR irradiation exhibited a slight dimming of red fluorescence and the appearance of green fluorescence, indicating that the mitochondria were affected by hyperthermia. For the cells with CDT treatment (GOD/CuFe-LDHs (pH 6.5)), a significant decrease in MMP was indicated by the strong green fluorescence of JC-1 monomers and weak red fluorescence of JC-1 aggregates, suggesting that the generation of large amounts of ˙OH led to mitochondrial damage. The depolarization of mitochondrial membranes was most pronounced in GOD/CuFe-LDHs (pH 6.5) in the NIR group, as evidenced by the further enhancement of green fluorescence and the disappearance of red fluorescence in cells, demonstrating the hyperthermia/˙OH-mediated mitochondrial dysfunction. These intriguing results demonstrated that the CDT-generated ˙OH and PTT-induced local hyperthermia could not only cause severe rupture of lysosomes but also induce the dysfunction of mitochondria. Lysosomal damage would result in the release of numerous proteolytic enzymes (such as caspases) that play an important role in the activation of cancer-cell apoptosis. Mitochondrial dysfunction can cause mitochondrial hypertonic state and directly lead to cell apoptosis. The synergistic lysosomal damage and mitochondrial dysfunction effectively promoted the therapeutic effect of GOD/CuFe-LDHs under NIR irradiation. Furthermore, cell apoptosis of the

treated Hela cells was analyzed by the annexin V-FITC/PI double staining method and the result is depicted in Fig. 4G. Hela cells incubated with GOD/CuFe-LDHs at pH = 7.4 under irradiation and at pH = 6.5 without irradiation indicated partial apoptosis. In the case of GOD/CuFe-LDHs at pH = 6.5 under irradiation, cell apoptosis occurred in both early and late stages with significant increment, demonstrating the effective synergetic PTT/CDT performance.

These exciting results *in vitro* encourage us to study the blood circulation, biodistribution, real-time imaging and tumor inhibition of GOD/CuFe-LDHs *in vivo*. Hela cells were subcutaneously injected into female BALB/c mice to establish a tumor-bearing mice model. The pharmacokinetics analysis of the GOD/CuFe-LDHs was conducted by measuring the Cu concentrations in blood at different time points post-injection. The fitting data (Fig. S14†) indicated that the blood circulation of GOD/CuFe-LDHs followed a typical two-compartment model, and the half-lives were 0.71 ± 0.06 h (distribution phase) and 11.08 ± 0.95 h (elimination phase) respectively, demonstrating the long blood circulation time of GOD/CuFe-LDHs.

Subsequently, the biodistribution of GOD/CuFe-LDHs was examined after intravenous injection, and the Cu concentrations in major organs (heart, liver, spleen, lungs, and kidneys) and tumors of mice were determined by inductively coupled plasma-mass spectrometry (ICP-MS). As shown in Fig. S15,† GOD/CuFe-LDHs could effectively accumulate at tumor sites and reached its highest value at about 12 h post-injection. The excellent accumulation of GOD/CuFe-LDHs at tumor sites can be attributed to the enhanced permeation and retention (EPR) effect. After that, an *in vivo* antitumor study was carried out to validate the potential of GOD/CuFe-LDHs for synergetic cancer therapy. 18 Hela tumor-bearing mice were separated into 3 groups at random when the tumors reached ~80 mm³: (1) PBS + NIR, (2) GOD/CuFe-LDHs, and (3) GOD/CuFe-LDHs + NIR. After intravenous administration of PBS or GOD/CuFe-LDHs (1 mg kg⁻¹, 200 µL), these mice were exposed to an 808 NIR (1.0 W cm⁻¹, 10 min) laser at 12 h post-injection. The tumor-site temperature of PBS-injected and GOD/CuFe-LDH-injected mice reached 37.3 and 53.6 °C respectively as monitored with an infrared thermal camera (Fig. 5A), demonstrating excellent
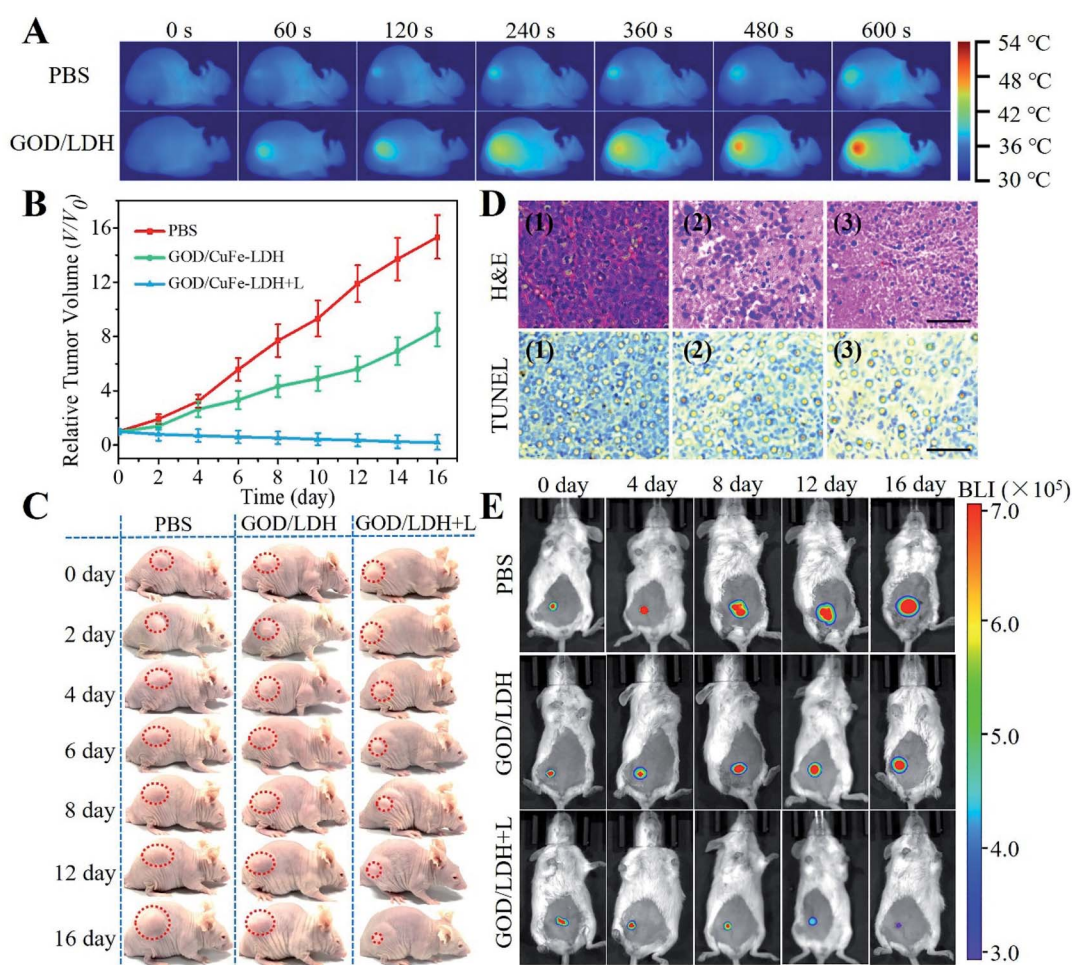

Fig. 5 (A) *In vivo* photothermal imaging of mice *i.v.* injected with PBS and GOD/CuFe-LDHs after 12 h with 10 min irradiation. (B) Hela tumor growth curves with various drug treatments (*$p < 0.05$, **$p < 0.01$). (C) Digital photographs of mice with various drug treatments at different time points. (D) H&E and TUNEL stained tumor tissue slices from different groups of mice after 16 d post-treatment. Scale bars are 100 µm. (E) Bioluminescence images of tumor-bearing mice post various treatments.

photothermal performance. To quantitatively evaluate the therapeutic effect, the tumor volume was recorded in the following 16 days of feeding (Fig. 5B). As a control, the PBS group with irradiation exhibited negligible tumor inhibition, and the GOD/CuFe-LDH group without irradiation inhibited tumor growth slightly, showing a certain level of CDT efficacy. However in the case of the GOD/CuFe-LDH group with irradiation, a significant tumor growth suppression was observed, indicating the synergistic CDT/PTT therapeutic effect of GOD/CuFe-LDHs. The digital photos of mice (Fig. 5C) and corresponding excised tumors (Fig. S16†) reflected the excellent antitumor effect of GOD/CuFe-LDHs with irradiation, which was consistent with the tumor volume curves. Moreover, the mice of each group maintained normal weight without obvious side effects (Fig. S17†). Hematoxylin and eosin (H&E) staining and TUNEL staining toward tumor slice revealed that the tumor tissue treated with GOD/CuFe-LDHs under irradiation was obviously necrotic, while the morphology of the remaining two groups was normal or partially necrotic (Fig. 5D). Furthermore, histological analysis, blood biochemistry, and liver, and kidney function markers, as well as H&E analysis of major organs, were used to assess the *in vivo* toxicity of GOD/CuFe-LDHs. Compared with the PBS group, the GOD/CuFe-LDH-treated group exhibited no statistical difference in all parameters, demonstrating that GOD/CuFe-LDHs caused no noticeable infection, inflammation or tissue damage (Fig. S18 and S19†). In addition, an *in situ* tumor model was further established and the bioluminescence imaging (BLI) was used to testify the synergistic CDT/PTT performance of GOD/CuFe-LDHs. It can be seen from Fig. 5E that the BLI signal observed in the GOD/CuFe-LDH group without irradiation decreased slightly on the 16th-day post-administration compared with the PBS group, displaying a certain degree of the CDT effect. For the GOD/CuFe-LDH group with irradiation, a weak BLI signal and significant tumor destruction were observed, thereby confirming the synergistic CDT/PTT therapeutic effect of GOD/CuFe-LDHs. The relative tumor volume of mice in Fig. S20† also confirmed this conclusion. Particularly, we examined the survival rates of different groups of mice after various treatments (Fig. S21†). Owing to tumor growth, all of the mice in the PBS group with irradiation and the GOD/CuFe-LDH group without irradiation died within 37 d and 48 d, respectively while the survival rate of mice in the GOD/CuFe-LDH group with irradiation is 100% within 60 d, illustrating the excellent synergistic CDT/PTT therapeutic effect of GOD/CuFe-LDHs.

Conclusions

In summary, with the combined advantage of acid-enhanced PTT and heat-facilitated CDT, GOD/CuFe-LDH ultrathin nanosheets could serve as a new type of TME-responsive theranostics system to eliminate tumors completely. CuFe-LDH nanosheets possessed a significant number of defects under acid conditions, leading to significantly acid-enhanced photothermal conversion. The PCE of GOD/CuFe-LDH nanosheets at pH = 6.5 and 5.4 was 75.1% and 83.2%, obviously higher than that of 46.0% at pH = 7.4. In addition, with a high velocity (V_{max} = 2.00

$\times 10^{-7}$ M) and low Michaelis–Menten constant (K_M = 12.01 mM), GOD/CuFe-LDH nanosheets displayed efficient ˙OH production in the TME. More importantly, the local heat generated from PTT accelerated the activity of the Fenton reaction, further improving the synergistic effect of PTT/CDT. Both *in vitro* and *in vivo* tests proved that GOD/CuFe-LDH nanosheets had an excellent antitumor effect. Therefore, this research provides a new pH-responsive nanoplatform based on GOD/CuFe-LDHs for CDT/PTT synergistic therapy.

Conflicts of interest

There are no conflicts to declare.

Ethical statement

All the animal procedures were performed by following the protocols approved by the China-Japan friendship Hospital Animal Research Center.

Acknowledgements

References

1 H. Lin, Y. Chen and J. Shi, *Chem. Soc. Rev.*, 2018, **47**, 1938–1958.

2 Q. A. Martin, R. L. Anderson, K. Narayan and M. P. MacManus, *Nat. Rev. Clin. Oncol.*, 2017, **14**, 32–44.

3 T. L. Bray, M. Salji, A. Brombin, A. M. Pérez-López, B. Rubio-Ruiz, L. C. A. Galbraith, E. E. Patton, H. Y. Leung and A. Unciti-Broceta, *Chem. Sci.*, 2018, **9**, 7354–7361.

4 M. P. Stewart, A. Sharei, X. Ding, G. Sahay, R. Langer and K. F. Jensen, *Nature*, 2016, **538**, 183–192.

5 C. Zhang, L. Yan, Z. Gu and Y. Zhao, *Chem. Sci.*, 2019, **10**, 6932–6943.

6 L. Peng, X. Mei, J. He, J. Xu, W. Zhang, R. Liang, M. Wei, D. G. Evans and X. Duan, *Adv. Mater.*, 2018, **30**, 1707389.

7 W. Chen, J. Ouyang, H. Liu, M. Chen, K. Zeng, J. Sheng, Z. Liu, Y. Han, L. Wang, J. Li, L. Deng, Y. N. Liu and S. Guo, *Adv. Mater.*, 2017, **29**, 1603864.

8 Y. Zhang, M. Leonard, Y. Shu, Y. Yang, D. Shu, P. Guo and X. Zhang, *ACS Nano*, 2017, **11**, 335–346.

9 C. Wang, W. Sun, G. Wright, A. Z. Wang and Z. Gu, *Adv. Mater.*, 2016, **28**, 8912–8920.

10 H. Pan, S. Li, J. Kan, L. Gong, C. Lin, W. Liu, D. Qi, K. Wang, X. Yan and J. Jiang, *Chem. Sci.*, 2019, **10**, 8246–8252.

11 Y. Xing, M. Xu, W. Ju, X. Luo, X. Hu, X. Liu, T. Kang, P. Wu, C. Cai and J. Zhu, *Chem. Sci.*, 2019, **10**, 10900–10910.

12 L. Zhang, Y. Zhang, Y. Xue, Y. Wu, Q. Wang, L. Xue, Z. Su and C. Zhang, *Adv. Mater.*, 2019, **31**, 1805936.

13 R. Xing, Q. Zou, C. Yuan, L. Zhao, R. Chang and X. Yan, *Adv. Mater.*, 2019, **31**, 1900822.

14 Y. Liu, P. Bhattarai, Z. Dai and X. Chen, *Chem. Soc. Rev.*, 2019, **48**, 2053–2108.

15 Z. Li, H. Huang, S. Tang, Y. Li, X. F. Yu, H. Wang, P. Li, Z. Sun, H. Zhang, C. Liu and P. K. Chu, *Biomaterials*, 2016, **74**, 144–154.

16 J. Peng, Y. Xiao, W. Li, Q. Yang, L. Tan, Y. Jia, Y. Qu and Z. Qian, *Adv. Sci.*, 2018, **5**, 1700891.

17 W. H. Chen, G. F. Luo, Q. Lei, S. Hong, W. X. Qiu, L. H. Liu, S. X. Cheng and X. Z. Zhang, *ACS Nano*, 2017, **11**, 1419–1431.

18 G. Reina, J. M. Gonzalez-Dominguez, A. Criado, E. Vazquez, A. Bianco and M. Prato, *Chem. Soc. Rev.*, 2017, **46**, 4400–4416.

19 W. P. Li, C. H. Su, Y. C. Chang, Y. J. Lin and C. S. Yeh, *ACS Nano*, 2016, **10**, 2017–2027.

20 Z. Tang, H. Zhang, Y. Liu, D. Ni, H. Zhang, J. Zhang, Z. Yao, M. He, J. Shi and W. Bu, *Adv. Mater.*, 2017, **29**, 1701683.

21 S. Dong, J. Xu, T. Jia, M. Xu, C. Zhong, G. Yang, J. Li, D. Yang, F. He, S. Gai, P. Yang and J. Lin, *Chem. Sci.*, 2019, **10**, 4259–4271.

22 L. Zhang, S. S. Wan, C. X. Li, L. Xu, H. Cheng and X. Z. Zhang, *Nano Lett.*, 2018, **18**, 7609–7618.

23 L. S. Lin, J. Song, L. Song, K. Ke, Y. Liu, Z. Zhou, Z. Shen, J. Li, Z. Yang, W. Tang, G. Niu, H. H. Yang and X. Chen, *Angew. Chem., Int. Ed.*, 2018, **57**, 4902–4906.

24 M. F. Poyton, A. M. Sendecki, X. Cong and P. S. Cremer, *J. Am. Chem. Soc.*, 2016, **138**, 1584–1590.

25 B. Ma, S. Wang, F. Liu, S. Zhang, J. Duan, Z. Li, Y. Kong, Y. Sang, H. Liu, W. Bu and L. Li, *J. Am. Chem. Soc.*, 2019, **141**, 849–857.

26 H. Zhao, Y. Wang, Y. Wang, T. Cao and G. Zhao, *Appl. Catal., B*, 2012, **125**, 120–127.

27 Q. Chen, C. Liang, X. Sun, J. Chen, Z. Yang, H. Zhao, L. Feng and Z. Liu, *PNAS*, 2017, **114**, 5343–5348.

28 R. Kumar, W. S. Shin, K. Sunwoo, W. Y. Kim, S. Koo, S. Bhuniya and J. S. Kim, *Chem. Soc. Rev.*, 2015, **44**, 6670–6683.

29 K. Zhang, X. Meng, Y. Cao, Z. Yang, H. Dong, Y. Zhang, H. Lu, Z. Shi and X. Zhang, *Adv. Funct. Mater.*, 2018, **28**, 1804634.

30 S. Guan, R. Liang, C. Li, D. Yan, M. Wei, D. G. Evans and X. Duan, *J. Mater. Chem. B*, 2016, **4**, 1331–1336.

31 X. Mei, J. Ma, X. Bai, X. Zhang, S. Zhang, R. Liang, M. Wei, D. G. Evans and X. Duan, *Chem. Sci.*, 2018, **9**, 5630–5639.

32 W. Liu, S. Xu, S. Guan, R. Liang, M. Wei, D. G. Evans and X. Duan, *Adv. Mater.*, 2018, **30**, 1704376.

33 Z. Yu, W. Hu, H. Zhao, X. Miao, Y. Guan, W. Cai, Z. Zeng, Q. Fan and T. T. Y. Tan, *Angew. Chem., Int. Ed.*, 2019, **58**, 8624–8628.

34 C. Liu, S. Zhang, J. Li, J. Wei, K. Mgllen and M. Yin, *Angew. Chem., Int. Ed.*, 2019, **58**, 1638–1642.

35 W. Zhen, Y. Liu, L. Lin, J. Bai, X. Jia, H. Tian and X. Jiang, *Angew. Chem., Int. Ed.*, 2018, **57**, 10466–10470.

36 Y. Cheng, Y. Chang, Y. Feng, H. Jian, Z. Tang and H. Zhang, *Angew. Chem., Int. Ed.*, 2018, **57**, 246–251.

37 J. Song, F. Wang, X. Yang, B. Ning, M. G. Harp, S. H. Culp, S. Hu, P. Huang, L. Nie, J. Chen and X. Chen, *J. Am. Chem. Soc.*, 2016, **138**, 7005–7015.

38 Y. Xuan, X. Q. Yang, Z. Y. Song, R. Y. Zhang, D. H. Zhao, X. L. Hou, X. L. Song, B. Liu, Y. D. Zhao and W. Chen, *Adv. Funct. Mater.*, 2019, **29**, 1900017.

39 J. Zhang, C. Yang, R. Zhang, R. Chen, Z. Zhang, W. Zhang, S. H. Peng, X. Chen, G. Liu, C. S. Hsu and C. S. Lee, *Adv. Funct. Mater.*, 2017, **27**, 1605094.

40 T. Dong, K. Wen, J. Chen, J. Xie, W. Fan, H. Ma, L. Yang, X. Wu, F. Xu, A. Peng and H. Huang, *Adv. Funct. Mater.*, 2018, **28**, 1800135.

41 D. Frenkel and B. Smit, *Understanding Molecular Simulation: From Algorithms to Applications*, Academic press, 2001, vol. 1.

42 T. Liu, W. Liu, M. Zhang, W. Yu, F. Gao, C. Li, S. B. Wang, J. Feng and X. Z. Zhang, *ACS Nano*, 2018, **12**, 12181–12192.

43 Y. Liu, W. Zhen, Y. Wang, J. Liu, L. Jin, T. Zhang, S. Zhang, Y. Zhao, S. Song, C. Li, J. Zhu, Y. Yang and H. Zhang, *Angew. Chem., Int. Ed.*, 2019, **58**, 2429–2434.

44 S. Wang, Z. Wang, G. Yu, Z. Zhou, O. Jacobson, Y. Liu, Y. Ma, F. Zhang, Z. Y. Chen and X. Chen, *Adv. Sci.*, 2019, **6**, 1801986.

45 L. S. Lin, T. Huang, J. Song, X. Y. Ou, Z. Wang, H. Deng, R. Tian, Y. Liu, J. F. Wang, Y. Liu, G. Yu, Z. Zhou, S. Wang, G. Niu, H. H. Yang and X. Chen, *J. Am. Chem. Soc.*, 2019, **141**, 9937–9945.

46 F. Zhang, X. Han, Y. Hu, S. Wang, S. Liu, X. Pan, H. Wang, J. Ma, W. Wang, S. Li, Q. Wu, H. Shen, X. Yu, Q. Yuan and H. Liu, *Adv. Sci.*, 2019, **6**, 1801507.

47 X. Wan, H. Zhong, W. Pan, Y. Li, Y. Chen, N. Li and B. Tang, *Angew. Chem.*, 2019, **131**, 14272–14277.

48 W. Feng, X. Han, R. Wang, X. Gao, P. Hu, W. Yue, Y. Chen and J. Shi, *Adv. Mater.*, 2019, **31**, 1805919.

49 B. Li, J. Tang, W. Chen, G. Hao, N. Kurniawan, Z. Gu and Z. Xu, *Biomaterials*, 2018, **177**, 40–51.